



Study of structural, surface morphology, Raman spectroscopy, and electrochemical properties of $\text{Bi}_{1+x}\text{FeO}_3$ nanoparticles for usage in supercapacitors

Garima Srivastava¹ · Shalendra Kumar² · S. Z. Hashmi³ · Ravina¹ · A. M. Quraishi⁴ · Saurabh Dalela⁵ · Faheem Ahmed⁶ · Kavita Kumari⁷ · B. H. Koo⁷ · P. A. Alvi¹

Received: 19 July 2023 / Accepted: 29 September 2023 / Published online: 25 October 2023
© The Author(s), under exclusive licence to Springer Science+Business Media, LLC, part of Springer Nature 2023

Abstract

This article reports the synthesis of $\text{Bi}_{1+x}\text{FeO}_3$ (with $x=0, 0.05, 0.10$) nanoparticles and their characterizing results for seeking the appropriate utility in making energy storage devices like supercapacitors. The BFO nanoparticles were synthesized via the sol–gel route and characterized by different techniques. The structural analysis was carried out by XRD along with Rietveld refinement, which gives information about the particle size, micro-strain and rhombohedral picture with the R3c space group. This study has confirmed that the BFO5 in single phase is the most optimized phase with the most stoichiometry as compared to pure BFO and BFO10. For surface morphology, FESEM along with EDAX technique was used. The Raman spectrometer with a 532 nm laser was used to study the vibrational modes available in the samples. To understand the super-capacitive behaviour of the synthesized samples, a detailed electrochemical analysis was performed with the help of cyclic-voltammetry. According to the recording of cyclic-voltammetry data for the samples BFO, BFO5, and BFO10 with the scan frequencies 10, 20, 50, and 100 mV/s, it was found that the BFO5 (i.e. $\text{Bi}_{1+x}\text{FeO}_3$ with $x=0.05$) electrode has displayed the highest capacitive reaction in comparison to the pure BFO and BFO10 electrodes. In addition, the BFO5 has shown the highest specific capacitance. The impedance analysis was also performed to study the grain properties of the samples via Nyquist plots considering the equivalent ac circuit, which confirmed that the BFO5 nanoparticles display the greatest grain resistance. Further, the justified Nyquist plots with the fitted data have confirmed the best performance of BFO5. According to the GCD (galvanostatic charge–discharge) study, the BFO5 electrode has demonstrated impressive cycle stability. As evaluated at 1Ag^{-1} , the BFO5 electrode has demonstrated outstanding cyclic stability, with $>94\%$ capacitance retention over 2000 cycles. Thus, in conclusion, all these characterization results suggest that the $\text{Bi}_{1+x}\text{FeO}_3$ with $x=0.05$ is a very suitable composition for supercapacitors application.

Keywords BFO · Nanomaterial · Structure · Raman spectroscopy · Supercapacitors

1 Introduction

In the last few decades, supercapacitors have become more popular due to their potential to one day replace batteries, which are very essential in cutting-edge technology (Vyas et al. 2022; Sheng et al. 2021; Sharma and Kumar 2020; Mauger et al. 2019). The design and manufacturing of supercapacitors can only be accomplished by studying electrode materials that have both a high energy density and electrochemical stability. Furthermore, these assets are used in a manner that benefits both the environment and the economy (Jadhav et al. 2016; Kumari et al. 2021a; Kumar et al. 2022). There has been a rise in awareness of the use of bismuth-based materials and composites for energy storage applications, including batteries and supercapacitors, because of their favourable redox behaviour, charge storage capacity, environmental friendliness, and low cost. However, after extensive studies on advanced materials like BFO, it has been confirmed that BFO sustains a perovskite structure and exhibits both ferroelectric and anti-ferromagnetic ordering. But, because of its poor insulating resistance, BFO is not often used in energy storage devices. Due to the material's limited temperature stability window, the production of pure single-phase BFO is crucial and challenging. Non-stoichiometry-related leakage current issues have prevented BiFeO_3 from making a big impact in the electronic sector since its discovery in 1960. As a result, a powder with a larger grain size is produced, and the process itself is not very repeatable in the case of supercapacitors (Kumar et al. 2021a). When precipitation and co-precipitation occur at the same time, a coarser powder is formed, which may lead to the production of an impurity phase or require a higher calcination temperature of 830°C . It is well recognized that the particle size, shape, and crystallinity of a photocatalyst have a significant impact on its activity (Al-Maswari et al. 2021). In recent years, many different techniques have been used to produce BFO particles with the desired morphologies. This is due to the fact that it has a period of 62 nm on its magnetic spin cycloid, which makes its magnetism somewhat weak at ambient temperature. So far, most research on BFOs has been conducted in the form of two-dimensional epitaxial thin films produced on a variety of substrates (Devi and Ray 2020). During this time, the crystal lattice structure, polarization, and magnetization undergo changes due to epitaxial strain. Recent research on supercapacitors, however, has focused not just on related nanoparticles, nanomaterials, and low-dimensional nanostructures but also on polycrystals (Moharana et al. 2021). Traditional solid-state methods for the synthesis of BFO nanoparticles have shown to have low reproducibility in supercapacitors, according to previous research (Bismibanu et al. 2018). As a byproduct of this process, coarser particles and an impurity phase of $\text{Bi}_2\text{O}_3/\text{Bi}_2\text{Fe}_4\text{O}_9$ are created. Producing BFO nanoparticles has so far been accomplished by a number of chemical techniques, such as simple solution technique, hydrothermal treatment, mechano-chemical synthesis, sol-gel method, and green synthesis (Wang et al. 2008, 2007, 2009, 2015; Biasotto et al. 2011; Wu et al. 2018; Cheema 2021; Kumar et al. 2021b; Choudhary et al. 2020; Matinise et al. 2023; Nayak and Gopalakrishnan 2022; Khajonrit et al. 2018; Bera et al. 2019; Kumari et al. 2021b). However, there are certain drawbacks to these methods, such as the risk of end-product contamination.

BFO's electrical and multiferroic characteristics are very susceptible to imperfections such as interstitials, vacancies, and secondary phases (Kock et al. 2008). The vast surface area of these imperfections means that even if they are small and undesirable in bulk, they have a considerable impact on changing the characteristics at the nanoscale. According to reported literature, defects such as oxygen vacancies are the primary causes of the abnormal electrical characteristics of oxide nanoparticles (Miriayala et al. 2013). As

a multiferroic material, the single phase BFO has greater promise since magnetoelectric coupling happens at ambient temperature. The impurities, which are visible as secondary phases, extend into three distinct zones. The first is the evaporation of the bismuth element, which is occurring with greater ease and as a result of the dissolved Bi-salt's lowering temperature due to the creation of Bi_2O_3 , $\text{Bi}_2\text{Fe}_4\text{O}_9$ and $\text{Bi}_{25}\text{FeO}_{39}$ two secondary phases are produced simultaneously with single-phase BFO. The third is the alteration of Fe ion chemical valence state in an oxygen-deficient environment. The maximal leakage current of BFO is typically referred to as this charge defect with regard to the Fe^{2+} ion produced during the synthesis (Kumari et al. 2014; Wu et al. 2016). Due to their increased power density and longer cycle, the BiFeO_3 based nano-structures are regarded as potentially active electrode materials for electrochemical supercapacitor applications, which suggest their prospective uses in an electric vehicle and portable electronics. Numerous groups have created nanostructures based on BiFeO_3 and worked to enhance their electrochemical characteristics. Although BiFeO_3 nanostructures and materials based on their composites have been employed as supercapacitor electrode materials. For thin films made of BiFeO_3 , Lokhande et al. observed that the specific capacitance was 81 F/g (Lokhande et al. 2007). To increase chemical stability, reduce oxygen vacancy concentration, and lower leakage current, rare-earth ions were substituted on the A or B site in ABO_3 type BFO. To lessen valence variations, which lowers the leakage current, transition metals were substituted on the B or Fe site. Due to the volatile nature of Bi, which causes oxygen vacancies to be produced, pure bismuth ferrite has big grains that make the ions diffuse more freely. In present work, the main emphasis on BFO is given just to maintain the optimization, stoichiometry and stability in secondary phases of BFO, as Bi by nature evaporates quickly during synthesis of sample. There will be the deficiency and sufficiency of bismuth in BFO and BFO10, respectively. Therefore, to avoid this, we took BFO5 as the standard.

The synthesis of BFO nanoparticles from a ferrioxalate precursor has been suggested by Ghosh et al. (Ghosh et al. 2005) as a method that involves heating a solution of certain salts to a temperature of 600 °C. In spite of the fact that the sintering temperature was raised in an effort to cut down on the number of impurities, a minute quantity of Bi_2O_3 was still found to be present in the end product. The synthesis of bismuth ferrites with controlled morphologies was accomplished by the use of a hydrothermal method (Manzoor et al. 2015). Although there were no traces of pollutants in the finished goods, the BFO nanoparticles that were created were sometimes of substantial size (reaching up to several hundred nanometers) (Rajaei et al. 2018). Thus, the goal was achieved by using a similar method. Hence, one can synthesize $\text{Bi}_2\text{Fe}_4\text{O}_9$ and $\text{Bi}_{25}\text{FeO}_4$ with zero impurity phases by making some minor adjustments to the amount of KOH that remains present. By using a nitrate-based variation of the Pechini technique, the researchers were able to produce BFO nanoparticles in the laboratory. In spite of the fact that this effort has succeeded in obtaining pure phase BFO, there was still some contamination owing to the fact that the precursor was broken down (Banerjee et al. 2019). In order to accomplish this goal, a gentle chemical approach was adopted.

At room temperature, the crystalline shape of the bismuth ferrite-ceramic mass exhibits a rhombohedral structure with $a = 5.63$ lattice constant and an 89.45° rhombohedral angle. Two polycrystalline cells with Fe^{3+} in the centre of FeO_6 octahedral and Bi^{3+} at the angular locations constitute the rhombohedral cells in this configuration. The hybridization of the Bi^{3+} lone pair and O_2 causes the Bi^{3+} to be displaced from centre locations, resulting in ferroelectric polarization across the (111) plane. The anti-ferromagnetic plane, which is perpendicular to the polarization direction, is formed by Fe^{3+} (Bhattacharyya et al. 2020). BFO is an excellent multiferroic nanomaterial with several distinctive features, including

large residual polarization, magnetoelectric coupling at ambient temperature, and a very small bandgap (Iriani and Sandi 2021; Kumari et al. 2020). As a result, it provides a diverse environment for experimenting with new methodologies. To increase ferroelectric property and magnetic efficiency, ion replacement, substrate selection, and the construction of morphotropic phase boundaries have all been employed (Wang et al. 2019; Zhang et al. 2018; Yan et al. 2010). The size effect-induced alteration of functions in BFO nanostructures is likewise of significant interest (Akbarzadeh et al. 2012). Efforts to improve performance have led to new applications in non-volatile storage, piezoelectric sensors, and photodetectors (Alharbi et al. 2019). However, various obstacles must be overcome before such revolutionary gadgets may be realized. First and foremost, it is critical to enhance ferroelectric and magnetoelectric performances. The BFO has high polarization. Second, it concerns the dynamical parameters. Dynamics can be stabilized, and the switching speed is met for devices that use ferroelectric or ferromagnetic switching. Most of the stated switching speeds and switching durability for universal memory are still unsatisfactory. As a result, using memory for BFO-based nanomaterials has been a long road (Kalikeri and Shetty Kodialbail 2021). Third, the physical processes of photovoltaic and photocatalytic behaviors in BFO nanoparticles remain a mystery. Only by elaborating on the physical mechanics can the scope of BFO photocatalysts and photovoltaic devices be expanded. Additionally, some other perovskite-structured nanoceramics such as $\text{Sr}_{0.5}\text{Ba}_{0.5}\text{Ti}_{1-x}\text{Fe}_x\text{O}_3$, (La^{3+}) Doped BaTiO_3 , and ZnFe_2O_4 have also been studied with unique properties for energy applications (Bhojar et al. 2020; Devmunde et al. 1644; Andhare et al. 1644). Further, Fe-doped TiO_2 nanocatalyst has been studied as promising candidate for industrial wastewater purification treatments (Somwanshi et al. 2021, 1644).

Various ideas have been offered; nevertheless, significant disagreements persist, and further research is required. More nanomaterial systems must be built in order to investigate the feasibility of developing novel devices and series of BFO. So, keeping in mind the above statements, in this article an effort has been made to elaborate on some of the properties of BFO nanoparticles that make them suitable for their utility in energy devices like supercapacitors.

2 Synthesis process

The $\text{Bi}_{1+x}\text{FeO}_3$ (with $x=0.00, 0.05, \text{ and } 0.10$) with 5% and 10% Bi excess nanoparticles were fabricated with a simple sol–gel route. By using the sol–gel process, one can synthesize various nanostructures, and this method is especially useful for the production of metal oxide nanoparticles. As the name of the method suggests, Sol (a colloidal solution) is created and gradually evolves towards the gel-like diphasic system (liquid and solid phases). In this typical synthesis, a solution of 0.1 M was prepared by $[\text{Bi}(\text{NO}_3)_3 \cdot 5\text{H}_2\text{O}]$ (AR 90.5%) and iron nitrate nonahydrate $[\text{Fe}(\text{NO}_3)_3 \cdot 9\text{H}_2\text{O}]$ (AR 99.5%) of Sigma Aldrich, respectively. The chemicals were weighed properly and utilized as a precursor for making a 0.1 M solution. A simple procedure has been used for the synthesis of the 0.1 M solution. Initially, citric acid ($\text{C}_6\text{H}_8\text{O}_7$) was used to make a solvent by dissolving in double-distilled water in a beaker. In the above solution, the ratio of citric acid and metal nitrate was kept at 1:1. Further, a small amount of concentrated nitric acid was used in order to amplify the dissolving solvent, followed by the addition of bismuth nitrate pentahydrate. Afterward, iron (III) nitrate nonahydrate was added to the above mixture to get the ratio of the compound in a proper mode. At the end, ethylene glycol was poured into the above mixture in a particular ratio and stirred at 90° to get a gel solution.

Next, the solution was vigorously stirred, which resulted in a light yellow-colored solution. The as-prepared samples were calcined at 550 °C for 2 h. Finally, a brown-coloured powder in precipitate form was obtained as the final product was obtained. The process sequence of the whole synthesis for synthesizing the Bi excess BFO ($\text{Bi}_{1+x}\text{FeO}_3$) nanostructures has been shown in the form of a flow chart, as revealed in Fig. 1. The governing electrochemical reactions for the preparation of BFO nanoparticles are mentioned below:



The following equations demonstrate the cathodic peak of Bi^{3+} to Bi_{metal} for the reduction process (discharging):

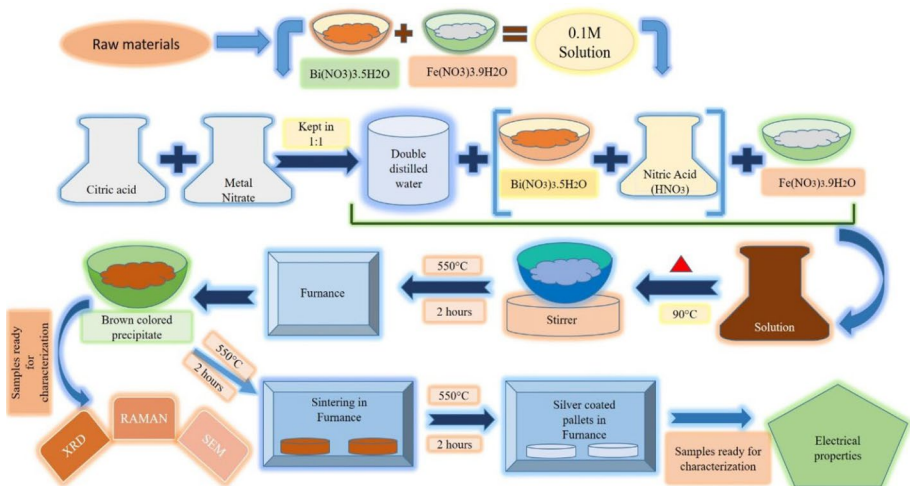
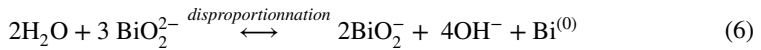
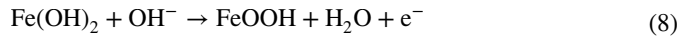


Fig. 1 Synthesis flow chart of Bi excess BFO via sol-gel route

The formation of oxidation peaks and reduction peaks in 1 mol KOH electrolytes is due to a redox process between Fe^{2+} and Fe^{3+} , which can be represented by the following equation (Li et al. 2017; Liu et al. 2014):



3 Characterizations

In order to study the various properties of the synthesized BFO nanoparticles and decide their appropriate applications in supercapacitors, different characterization techniques have been used. For phase identification, crystalline size, and micro-strain determination, the XRD (X-ray diffraction) technique was used. FESEM (field emission scanning electron microscope) was used to study the surface morphology. The cyclic voltammetry and electrochemical impedance spectroscopy techniques were used to measure the supercapacitive behaviour of the synthesized samples. For measuring the existing Raman bands in the samples, Raman spectroscopy was used.

3.1 XRD analysis

In Fig. 2, the XRD patterns of the synthesized BFO nanoparticles have been shown and the crystallite size of $\text{Bi}_{1+x}\text{FeO}_3$ ($x=0.00, 0.05, 0.10$) have been examined via XRD results. Figure 2 shows the XRD patterns of BFO powders annealed at 550 °C for 2 h. The presence of a secondary (impurity) phase i.e., $\text{Bi}_2\text{Fe}_4\text{O}_9$ has been observed along with BFO as

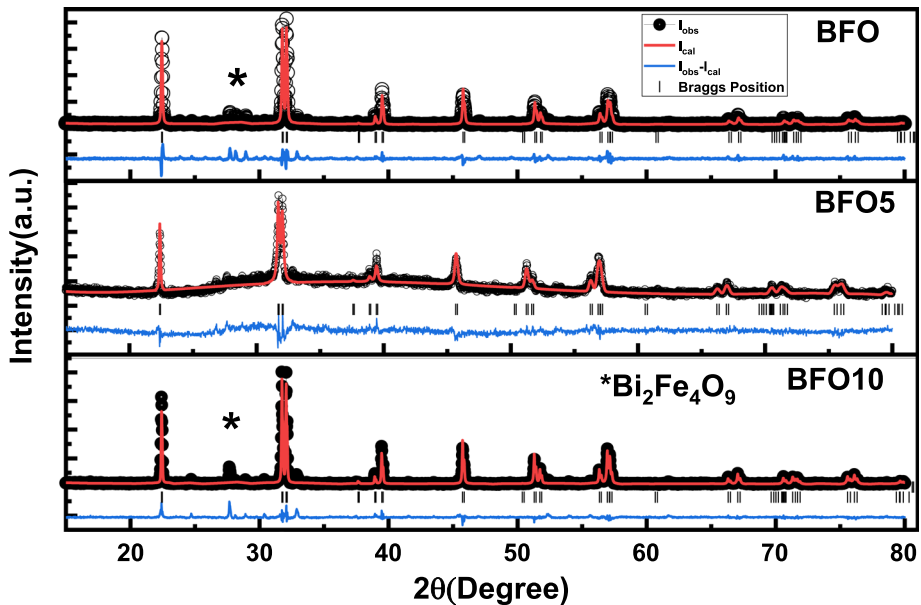


Fig. 2 XRD patterns of pure BFO, BFO5, BFO10. Samples were refined using the Rietveld method. $\text{Bi}_2\text{Fe}_4\text{O}_9$ impurity phase peaks are denoted by an asterisk (*)

the major phase during synthesis. Refer to Fig. 2, the most prominent peaks confirm the presence of BFO but some other peaks at low intensity also show by product $\text{Bi}_2\text{Fe}_4\text{O}_9$ located at $2\theta=27.81, 28.32, 29.00$. The secondary peaks can be attributed to the Bi^{3+} ion volatilizations that occur as a result of the further bismuth addition. Bi^{3+} ions tend to evaporate quickly during synthesis under conditions like drying and annealing in the bismuth excess series of BFO due to bismuth's greater vapor pressure. The peaks of the secondary phase $\text{Bi}_2\text{Fe}_4\text{O}_9$ increase as an increase in the doping percentage of Bi. BFO10 nanoparticles show a maximum fraction of secondary peak. While BFO5 and BFO at lower Bi content show the minimum fraction of the secondary phase. The sharp peaks indicate the crystalline nature of the material. The highest peak intensity was found at $2\theta=32.28, 32.26, 31.91$ for BFO, BFO5, and BFO10, respectively.

The average crystallite size was calculated by the Debye Scherrer formula (Scherrer 1918; Dangi et al. 2022; Khichar et al. 2020; Dhayal et al. 2020; Sharma et al. 2019):

$$D = \frac{k\lambda}{\beta\cos\theta} \quad (9)$$

In the above equation, k is a Scherrer constant (~ 0.98); β is peak width at half maximum intensity, and λ is the wavelength of the radiations (~ 1.540 nm). The calculated average crystallite size was determined as ~ 57 nm, 44 nm, 54 nm for pure BFO, BFO5, and BFO10, respectively. There was found a slight decrease in the sizes with increasing Bi doping at Bi sites in pure BFO. The sharp peaks indicate about the crystalline nature of the material. However, the peak broadening of the nano-particles due to lattice strain (ϵ) can be obtained with the help of FWHM (full width at half maximum: β) which can be expressed by W–H (Williamson Hall) relation (Mote et al. 2012; Kibasomba et al. 2018), as given below:

$$\frac{\beta\cos\theta}{\lambda} = \frac{1}{d} + \frac{\epsilon\sin\theta}{\lambda} \quad (10)$$

With the help of W–H plots, shown in Fig. 3 (a, b and c), it can clearly be seen that particles size decreases with increasing Bi doping. The different sizes of the nano-particles can cause stress which hinders crystalline growth. Calculations were performed to show that the structural parameter strain firstly increases and then decreases with the Bi excess. The parameters of micro-strain from the W–H plot were calculated as 0.04275, 0.06119, and 0.0546 for pure BFO, BFO5, and BFO10 nanoparticles, respectively. The extra addition of Bismuth results in the volatilization of Bi^{3+} which is assured with secondary peaks. Bi^{3+} ions get quickly evaporate during synthesis due to the higher vapor pressure of Bi, such as drying and annealing conditions in Bi excess series of BFO.

Refer to Fig. 2, utilizing the Rietveld refinement code included in the Fullproof open-access software, the XRD data were precisely examined. The XRD profile of the examined materials is depicted in Fig. 2. where the little black dots stand in for the experimental XRD pattern and the fine red lines represent the fitting curves with (χ^2) values 3.9, 2.1 and 2.8 for BFO, BFO5, BFO10, respectively. The blue line shows the difference between the measured and fit patterns, while the black vertical lines show exactly where the Bragg angles are located. All samples of Bi excess $\text{Bi}_{1+x}\text{FeO}_3$ are formed in rhombohedral distorted perovskite structure with R3c space group, as shown by the well matching between experimental and computed diffraction peaks. According to JCPDS card No. 01–074–1098, the extra weak peak at $2\theta=28^\circ$ may have been caused by the presence of a minor secondary phase of $\text{Bi}_2\text{Fe}_4\text{O}_9$. The peak positions show an apparent splitting along with the

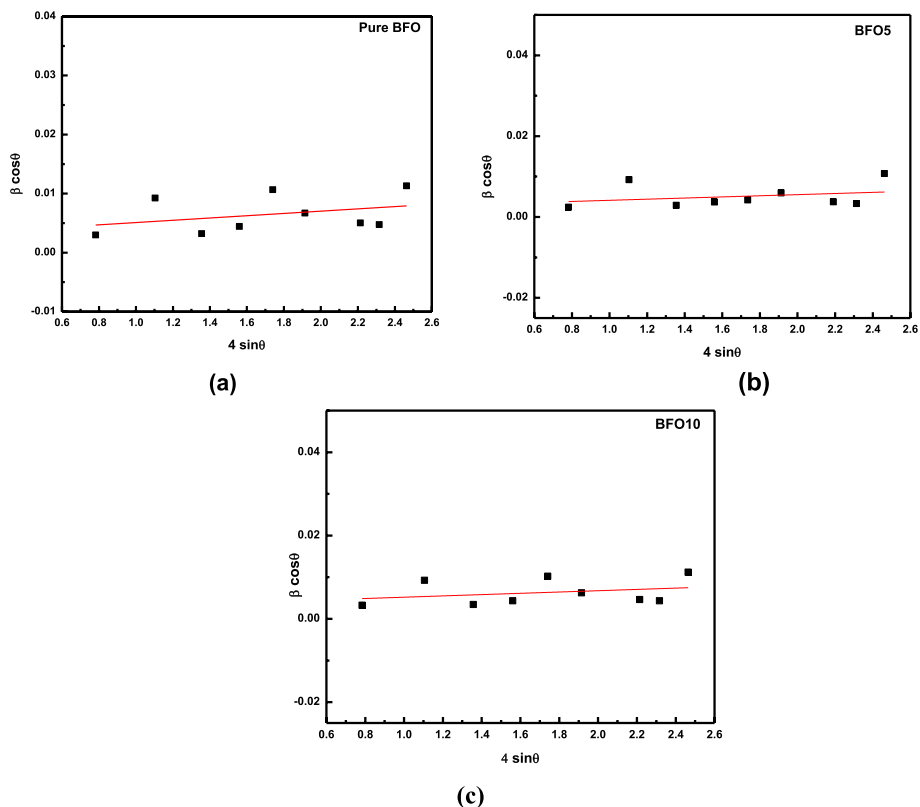


Fig. 3 W–H plot of **a** pure BFO; **b** BFO5; and **c** BFO10

reduced intensity and indicate a rhombohedral picture with the R3c space group having unit cell parameters of $a=b=5.579 \text{ \AA}$, $c=13.8705 \text{ \AA}$ and $\alpha=\beta=\gamma=90$.

3.2 Surface analysis

Analysis of surface morphology is very helpful in assessing the change in morphology, along with grain size and shape, that the introduction of the Bi-excess causes. In Fig. 4 (a, b, and c), FESEM images of pure BFO, BFO5, and BFO10 have been displayed, which illustrate the morphological properties of as-synthesized pure and Bi-doped BiFeO_3 nanoparticles. In Fig. 5, the FESEM mapping images and EDAX spectra showing elements presence in pure BFO, BFO5 and BFO10 have been illustrated. All particles are homogeneous and agglomerated. Agglomeration occurs as a result of surface attractive interactions and van der Waals forces, which are always present but only become significant at the nanoscale, where objects can get as close as nanometers to one another. However, as far as the drying process is concerned within the simple preparation, this agglomeration could potentially exist due to their high surface energy. Analysis performed by FESEM shows the spherical shape morphology of all the particles and gives information about the Bi excess nanoparticles composed of nano-crystalline grains. A high voltage (order 15 kV) was used for scanning the BFO, BFO5, and BFO10 nanoparticles, respectively.

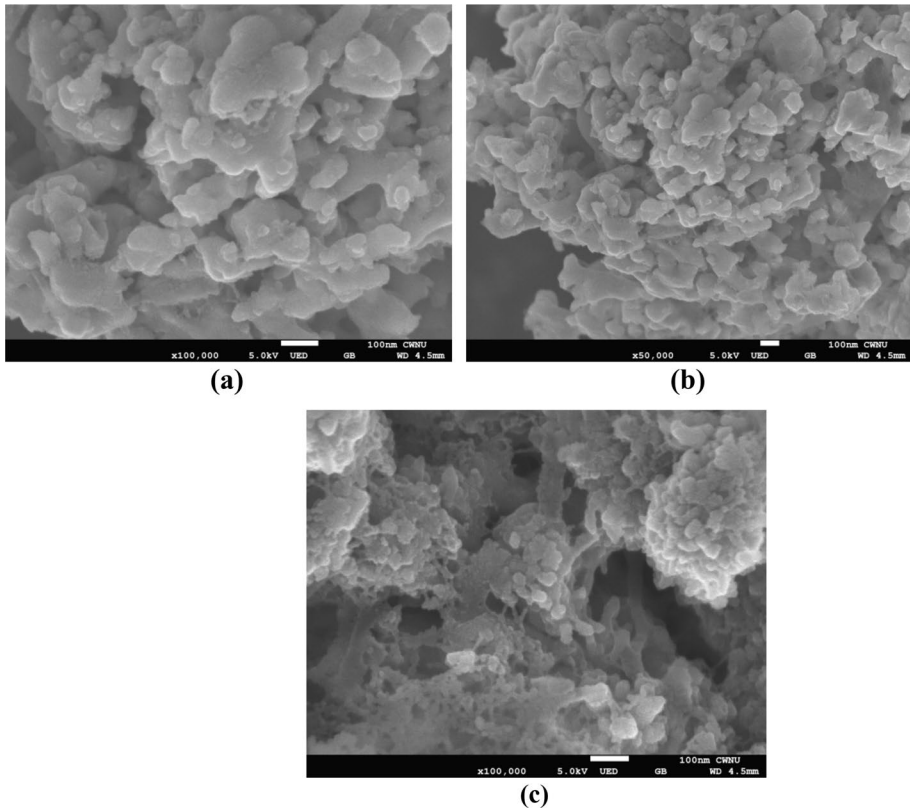


Fig. 4 FESEM images of **a** pure BFO **b** BFO5 **c** BFO10

3.3 C–V analysis

The cyclic-voltammetry (CV) analysis of $\text{Bi}_{1+x}\text{FeO}_3$ (with $x=0.00, 0.05$ and 0.10) with pure and 5% and 10% Bi excess nanoparticles for potential application in supercapacitors was carried out. There were three electrodes in the C–V setup. By using the cyclic-voltammetry, the calculations of the specific capacitance of the electrodes were performed from the mathematical relation given below (Iqbal et al. 2018):

$$C_{sp} = \frac{\int I.dV}{mK(V_2 - V_1)} \quad (11)$$

In the above expression, the integral part represents the area of the volumetric curve, m represents the mass of the material under investigation, the term $(V_2 - V_1)$ is used to represent the potential window and K is the scan rate.

The working electrodes were created by combining 80% active materials (BiFeO_3 , $\text{Bi}_{1.05}\text{FeO}_3$, and $\text{Bi}_{1.10}\text{FeO}_3$), 10% carbon black, and 10% polyvinylidene fluoride (PVDF). To create a slurry, the weighted electrode components were uniformly blended with *n*-methyl-2 pyrrolidinone (NMP) acting as the solvent. The slurry was applied to the nickel foam substrate (about 1.0 cm^2) and allowed to dry for 12 h at 80°C in the

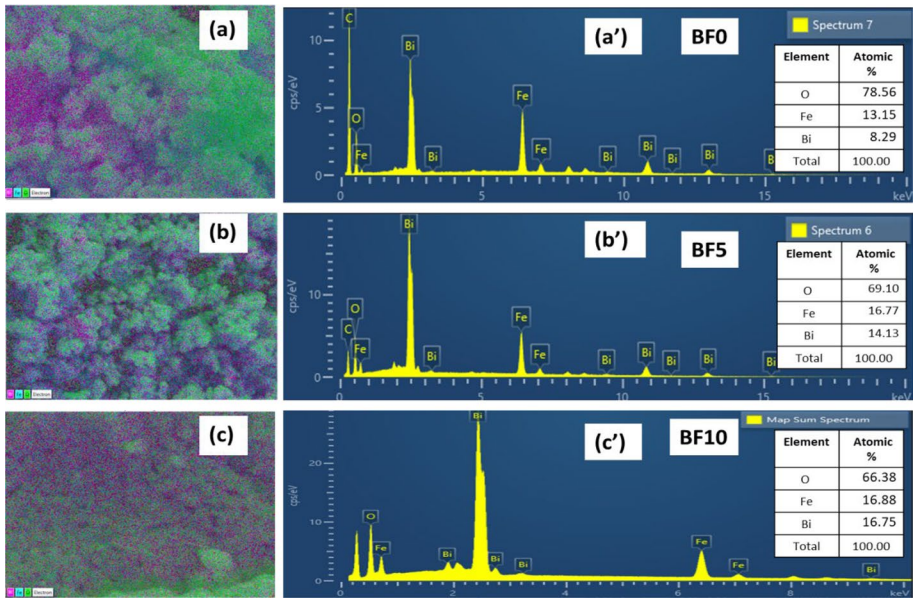


Fig. 5 FESEM mapping images and EDAX spectra of (a, a') pure BFO (b, b') BFO5 (c, c') BFO10

hot air oven. The weight of the active material Bi was 1 mg. In shape and size all the electrodes were identical. Pt and Ag/AgCl wires were used as reference and counter electrodes, respectively.

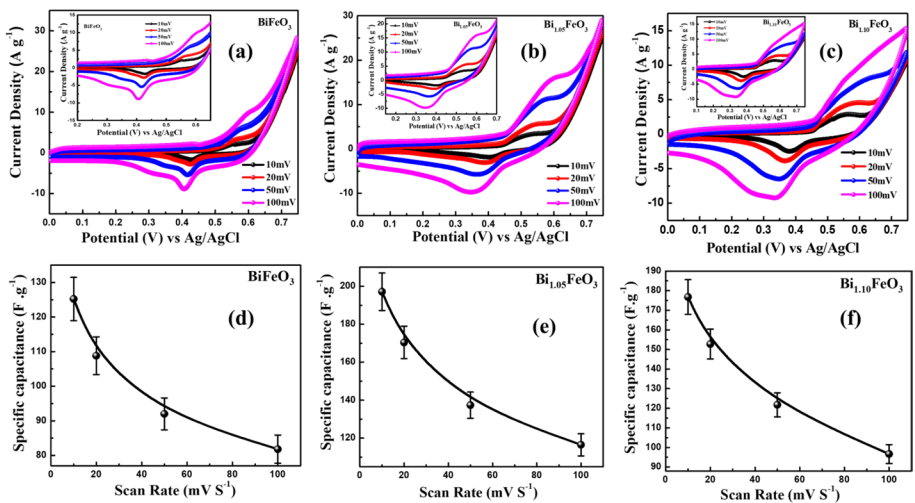


Fig. 6 (a, b and c) shows C–V plots of BFO; BFO5 and BFO10, respectively at scan frequencies of 10, 20, 50, and 100 mV/s; (d, e and f) shows the variations in specific capacitance (C_{sp}) of BFO, BFO5 and BFO10, respectively, with the different scan rate

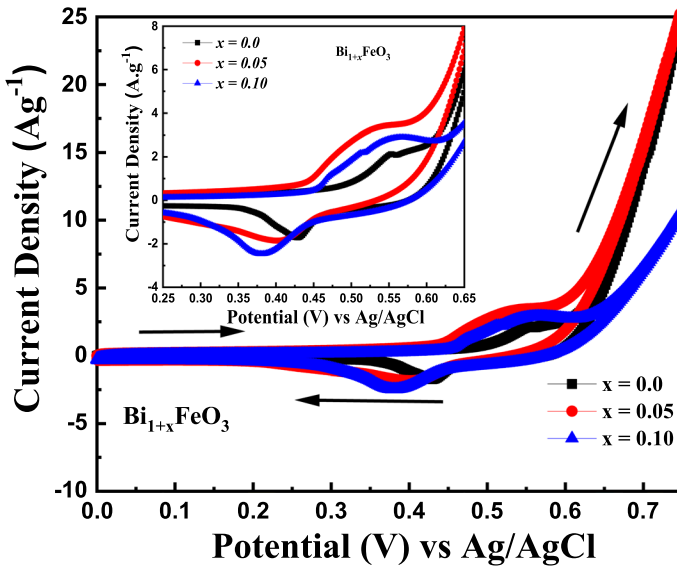


Fig. 7 C–V plot of $\text{Bi}_{1+x}\text{FeO}_3$ (with $x=0.00, 0.05$ and 0.10) nanoparticles at a particular scan frequency 10 mV/s

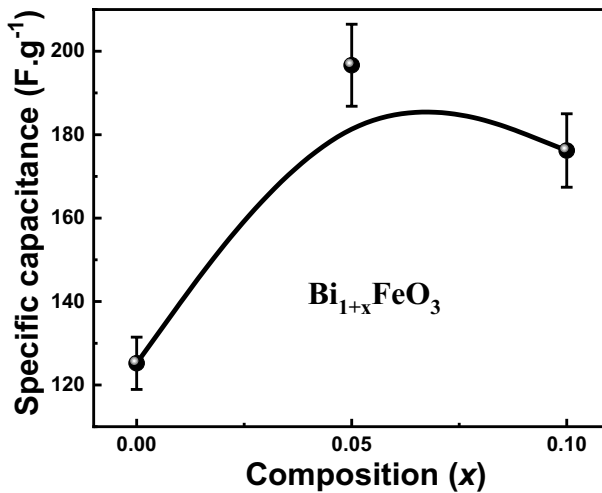


Fig. 8 Variations of specific capacitance (C_{sp}) due to change in composition

In Figs. 6 a–c, the recording of cyclic-voltammetry data for the samples BFO, BFO5, and BFO10 with the scan frequencies 10, 20, 50, and 100 mV/s has been shown. In Fig. 6a–c, the C (current density) Versus V (potential applied) curves (i.e., C–V curves) were plotted for BFO, BFO5, and BFO10, respectively, for the scan rate having range ranging from 10 to 100 mV/s . Further, the response of scan rate to the specific capacitance of BFO, BFO5, and BFO10 was shown in Figs. 6d–f. Moreover, C–V curves for different

compositions in $\text{Bi}_{1+x}\text{FeO}_3$ have been plotted in Fig. 7, and the response of change in composition to the specific capacitance has been illustrated in Fig. 8. From these plots, it is clear that the redox peaks of all the samples appear in the C–V curves, and the BFO5-based electrode showed the largest region in the C–V plot, as shown in Fig. 6b. The BFO5 electrode has displayed the highest capacitive reaction in comparison to the BFO and BFO10 electrodes. A numerical comparison of $\text{Bi}_{1+x}\text{FeO}_3$ (with $x=0.00, 0.05$ and 0.10) has been made in context of specific capacitance, current density, scan rates and electrolyte in Table 1. All investigated electrodes have shown redox peaks in the C–V curves due to the transition between different valence states. In electrolyte solution, only the outer sites could be more active at a higher scan rate than the inner sites, which completely inhibited the redox reaction. With increasing Bi doping concentration, the particle size gets reduced, which was observed from the XRD study, due to which an electrochemical reaction takes place with enhanced active surface area. From Figs. 6d–f, it can be predicted that the specific capacitance decreases for all samples with increasing scan rates (see Table 1).

3.4 Analysis of Raman spectroscopy

The as-prepared samples BFO, BFO5, and BFO10 synthesized via a simple sol–gel route were analyzed via Raman Spectrometer (Thermo Fisher) using a 532 nm diode laser. The vibrational modes studied through Raman Spectroscopy are shown in Fig. 9a, b and c. The vibrational modes for BFO were found at 336,373,411, and 697 cm^{-1} . For BFO5, the Raman active modes were found at 376,409,701 cm^{-1} , and; for BFO10 the modes were available at 375,409, and 702 cm^{-1} . Since the BFO is an R3c structure, hence the Raman active vibrational mode for BFO is 13 i.e. (4A1 + 9E). A1 modes are polarized along the z-plane whereas E mode is polarized along the X–Y plane; while A2 modes are silent. However, out of the 13 vibrational modes, there are 8 phonon modes. From Fig. 9, it can clearly be seen that A1-4 modes were available at 411 and 409 for BFO and BFO5, and BFO10, respectively. Other phonon modes were found at 375, and 376 cm^{-1} for BFO and BFO5, and BFO10, respectively.

3.5 Impedance analysis

The effect of the grain and grain boundary resistance to the total resistance of all the samples (BFO, BFO5, and BFO10) were further studied via Nyquist plots/ cole–cole plots as shown in Fig. 10. A graph is plotted between real impedance (Z') and imaginary impedance (Z''). Semicircular arcs in the graph are the results of high resistance at low frequency. Hence, the grain boundary of the nanoparticles is mostly identical complete resistance of the sample. Additionally, it can be seen that with increasing Bi-excess the diameter of the

Table 1 Comparison table of $\text{Bi}_{1+x}\text{FeO}_3$ (with $x=0.00, 0.05$ and 0.10)

Electrode material compositions	Scan rate (mV/s)	Specific capacitance (F/g)	Current density (A/g)	Electrolytes
BiFeO_3	10–100	125–82	0–25 A/g	1 Mol KOH
$\text{Bi}_{1.05}\text{FeO}_3$	10–100	198–118	0–30 A/g	1 Mol KOH
$\text{Bi}_{1.10}\text{FeO}_3$	10–100	178–95	0–15 A/g	1 Mol KOH

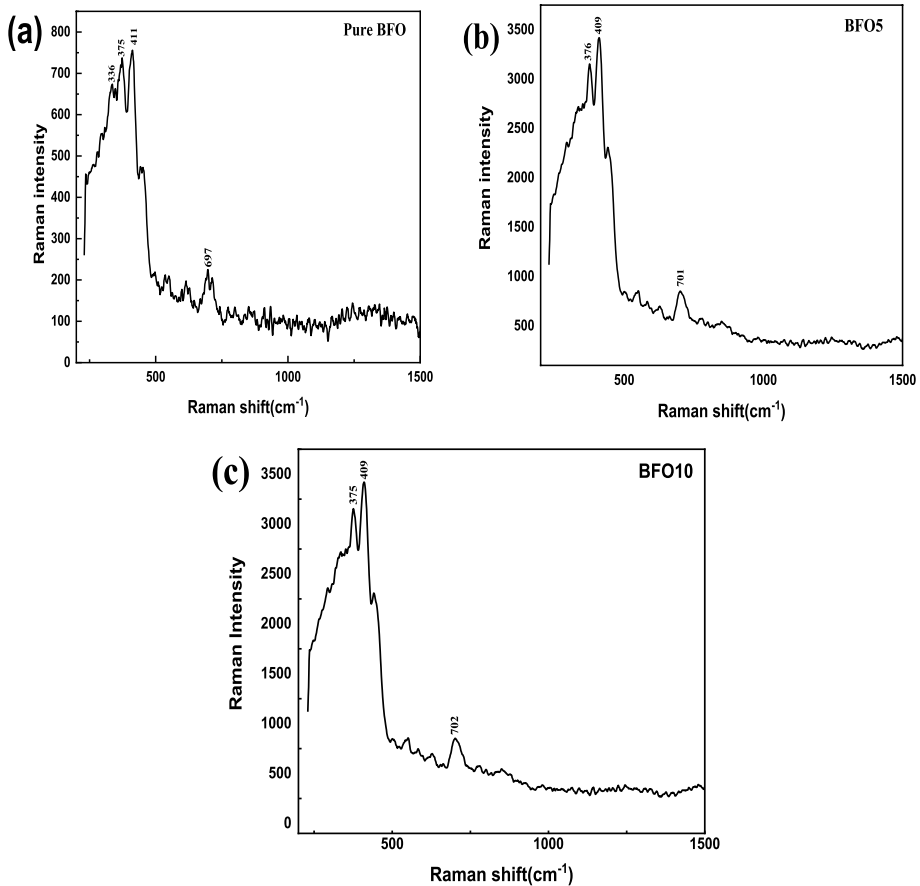


Fig. 9 Raman spectra for **a** BFO **b** BFO5, and **c** BFO10 nanoparticles

semicircles gets larger than that of the BFO and is found to be at its greatest for BFO. This implies that BFO nanoparticles display the greatest grain resistance.

EIS (electrochemical impedance spectroscopy) is quantitatively examined to glean more knowledge about the electrode material and electrolyte's electrical and ionic conductivity. Figure 10 displays the Nyquist plots for the $\text{Bi}_{1+x}\text{FeO}_3$ nanoparticles (where $x=0, 0.05,$ and 0.10) series samples fitted with the help of Zview software. The justified plots with the fitted data shown in Fig. 10 confirm the best performance of BFO5. Further, the EIS research was carried out at an open circuit potential with amplitude of 10 mV and an AC frequency range of 10 kHz to 1 MHz. Different parameters, such as solution resistance (R_s), charge transfer resistance (R_{ct}), Warburg impedance (W), and fitted parameters were used to fit the experimental data of the Nyquist plot. Since the ions do not have enough time to pass through the bulk of the electrode, the Nyquist plot exhibits a tiny arc that compensates for the charge transfer reactions and double-layer capacitance at the electrode/electrolyte interface. The R_{ct} values, which are 0.18, 5.1, and 1.69 for the BFO, BFO5, and BFO10 samples, respectively, depend on the semicircle's diameter. The equivalent circuit has been shown in inset of Fig. 10. From the equivalent circuit, the values of solution

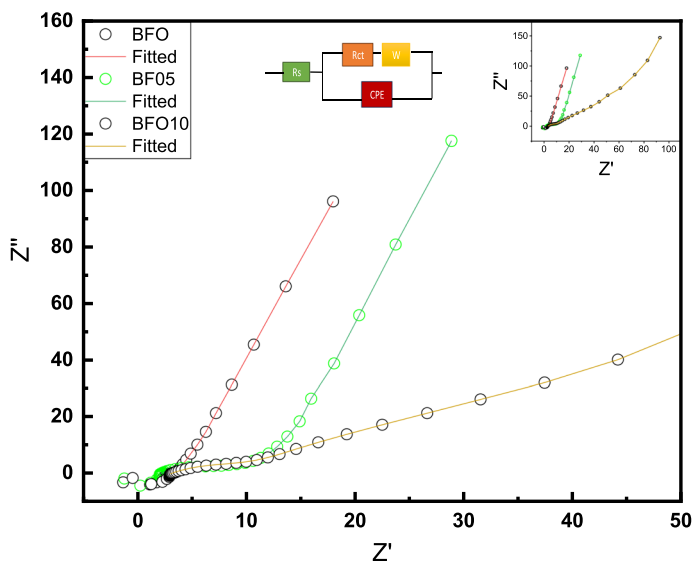


Fig. 10 Nyquist plots/Cole–Cole plots of BFO, BFO5 and BFO10 electrodes with fitted equivalent circuit

resistance (R_s) for BFO, BFO5 and BFO10 have been kept as 2.702, 2.109, and 3.074 Ω , respectively.

3.6 GCD (Galvanostatic charge–discharge) Study

Figure 11a shows that the specific capacitance is dropped as the current density increased. The specific capacitance was found to be $\sim 190 \text{ F g}^{-1}$ at 1 Ag^{-1} current density and dropped to $\sim 108 \text{ F g}^{-1}$ at 5 Ag^{-1} . Figure 11b shows that the specific capacitance dropped as the current density increased. The cycling behavior of the BFO5 electrode was carried out for 2000 cycles to examine the cyclic stability of the electrode, as shown in Fig. 11c. Figure 11c displays that with extensive cycling (more than 1000 cycles), just a very slight drop (6%) in the specific capacitance is visible, indicating no discernible fade. The BFO5 electrode has demonstrated impressive cycle stability. As evaluated at 1 Ag^{-1} , the BFO5 electrode has also demonstrated outstanding cyclic stability, with $> 94\%$ capacitance retention over 2000 cycles.

4 Summary and conclusion

The synthesis of $\text{Bi}_{1+x}\text{FeO}_3$ (with $x=0, 0.05, 0.10$) nanoparticles and their characterizations for seeking the suitable utility in making energy storage devices like supercapacitors have been performed. The best composition of $\text{Bi}_{1+x}\text{FeO}_3$ has been optimized for ($x=0.05$) with the help of structural analysis utilizing the XRD, Rietveld refinement, cyclic-voltammetry technique, impedance analysis and GCD study. It has been found that BFO5 in single phase is the most optimized phase which is almost stoichiometry as compared to pure BFO and BFO10. As in nature the Bi- evaporates out during

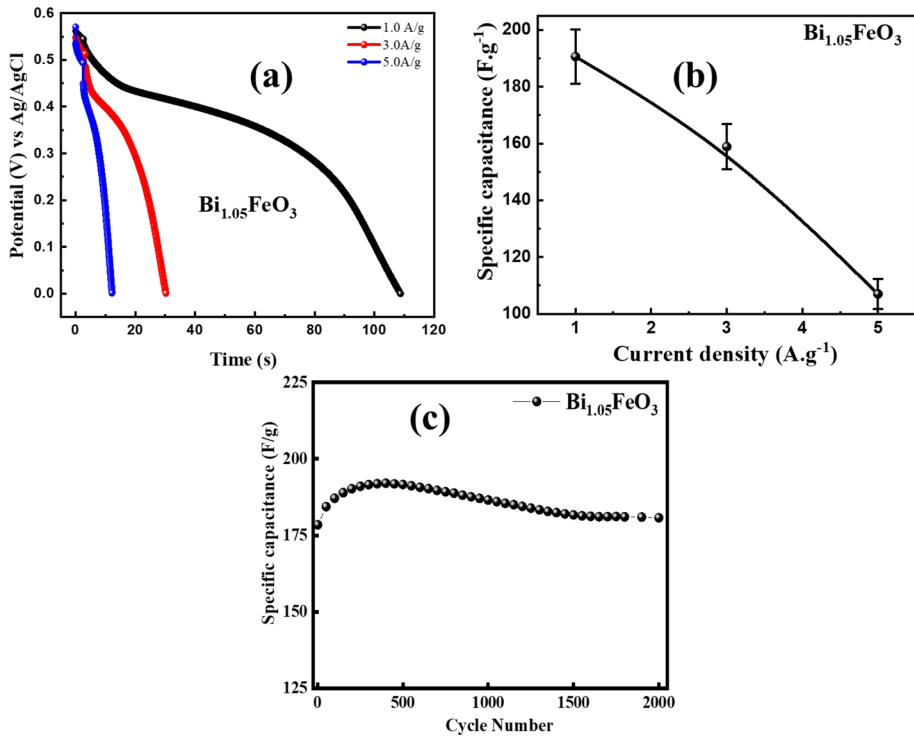


Fig. 11 **a** BFO5 discharge curves at various current densities. **b** Variation of the BFO5 electrode's specific capacitance with various current densities at 10 mV/s. **c** The BFO5 electrode's cycling performance at 1 Ag⁻¹ for 2000 cycles

synthesis, so, in pure BFO Bi- deficiency occurs while in BFO10 there is a sufficiency of Bi- and due to this volatile behavior, BFO show secondary phases. To compensate this deficiency and sufficiency in pure BFO and BFO10, the BFO5 have showed the optimized, stable and pure phase. The super-capacitive performance of the BFO5 has also been optimized by electrochemical analysis with the help of cyclic-voltammetry which has recorded the data for the samples of pure BFO, BFO5, and BFO10 with the scan frequencies 10, 20, 50, and 100 mV/s. It was found that the BFO5 (i.e. $\text{Bi}_{1+x}\text{FeO}_3$ with $x=0.05$) electrode has displayed the highest capacitive reaction in comparison to the BFO and BFO10 electrodes. In addition, the BFO5 has shown the highest specific capacitance. The impedance analysis has also been performed via Nyquist plots considering the equivalent ac circuit, which confirmed that the BFO5 nanoparticles display the greatest grain resistance. Further, the justified Nyquist plots with the fitted data have confirmed the best performance of BFO5. According to the GCD plots, the BFO5 electrode has demonstrated impressive cycle stability. As evaluated at 1Ag⁻¹, the BFO5 electrode has demonstrated outstanding cyclic stability, with > 94% capacitance retention over 2000 cycles. Thus, in conclusion, all these characterization results suggest that the BFO5 (i.e. $\text{Bi}_{1+x}\text{FeO}_3$ with $x=0.05$) is the best material for usage in energy storage application.

Acknowledgements The DST, Govt. of India is acknowledged by the authors: P. A. Alvi, Garima Srivastava, and Ravina, for awarding the CURIE project to Banasthali Vidyapith, Rajasthan.

Author contributions All authors contributed to the study conception and design. Data generation, collection and analysis were performed by [GS], [PAA], [SK], and [R]. The first draft of the manuscript was written by [GS], [PAA], [SZH], [FA], [KK], [BHK] and [AMQ] and all other authors commented on previous versions of the manuscript. All authors read and approved the final manuscript.

Data availability No data was used.

Declarations

Conflict of interest The authors declare that they have no conflict of interest.

Ethical approval Not applicable.

References

- Akbarzadeh, A., Samiei, M., Davaran, S.: Magnetic nanoparticles: preparation, physical properties, and applications in biomedicine. *Nanoscale Res. Lett.* **7**(1), 1–13 (2012)
- Alharbi, T.M., Al-Antaki, A.H., Moussa, M., Hutchison, W.D., Raston, C.L.: Three-step-in-one synthesis of supercapacitor MWCNT superparamagnetic magnetite composite material under flow. *Nanoscale Adv.* **1**(9), 3761–3770 (2019)
- Al-Maswari, B.M., Ahmed, J., Alzaqri, N., Ahamad, T., Mao, Y., Hezam, A., Venkatesha, B.M.: Synthesis of perovskite bismuth ferrite embedded nitrogen-doped carbon (BiFeO₃-NC) nanocomposite for energy storage application. *J. Energ. Storage* **44**, 103515 (2021)
- Andhare, D.D., Jadhav, S.A., M.V. Khedkar, Sandeep, B. S., More, S. D., Jadhav, K. M.: Structural and chemical properties of ZnFe₂O₄ nanoparticles synthesised by chemical co-precipitation technique. In: *Journal of Physics: Conference series*, vol. 1644, no. 1, pp. 012014. IOP Publishing (2020)
- Banerjee, M., Mukherjee, A., Chakrabarty, S., Basu, S., Pal, M.: Bismuth-doped nickel ferrite nanoparticles for room temperature memory devices. *ACS Appl. Nano Mater.* **2**(12), 7795–7802 (2019)
- Bera, K.K., Chakraborty, M., Chowdhury, S.R., Ray, A., Das, S., Bhattacharya, S.K.: Significantly improved and synergistic effect of Pt–ZnO–Bi₂O₃ ternary hetero-junctions toward anode-catalytic oxidation of methanol in alkali. *Electrochim. Acta* **322**, 134775 (2019)
- Bhattacharyya, A., Seth, G.S., Kumar, R., Chamkha, A.J.: Simulation of Cattaneo–Christov heat flux on the flow of single and multi-walled carbon nanotubes between two stretchable coaxial rotating disks. *J. Therm. Anal. Calorim.* **139**(3), 1655–1670 (2020)
- Bhojar, D.N., Somvanshi, S.B., Kharat, P.B., Pandit, A.A., Jadhav, K.M.: Structural, infrared, magnetic and ferroelectric properties of Sr_{0.5}Ba_{0.5}Ti_{1-x}Fe_xO₃ nanoceramics: modifications via trivalent Fe ion doping. *Phys. B: Condens. Matter* **581**, 411944 (2020)
- Biasotto, G., Simões, A.Z., Foschini, C.R., Zaghete, M.A., Varela, José A., Longo, E.: Microwave-hydrothermal synthesis of perovskite bismuth ferrite nanoparticles. *Mater. Res. Bull.* **46**(12), 2543–2547 (2011)
- Bismibanu, A., Alagar, M., Mercy-Jebaselvi, J.S., Gayathri, C.: Preparation and characterization of bismuth ferrite nanoparticle using sol–gel method. *Int. J. Res. Appl. Sci. Eng. Technol.* **6**(4), 1767–1770 (2018)
- Cheema, H., Yadav, V., Maurya, R.S., Yadav, V., Kumar, A., Sharma, N., Alvi, P.A., Kumar, U.: Structural, optical and electrical properties of Mn-doped ZnFe₂O₄ synthesized using sol–gel method. *J. Mater. Sci.: Mater. Electron.* **32**(18), 23578–23600 (2021)
- Choudhary, B.L., Kumar, U., Kumar, S., Chander, S., Sudhish, K., Dalela, S., Dolia, S.N., Alvi, P.A.: Irreversible magnetic behavior with temperature variation of Ni_{0.5}Co_{0.5}Fe₂O₄ nanoparticles. *J. Magn. Magn. Mater.* **507**, 166861 (2020)
- Dangi, S.B., Hashmi, S.Z., Upendra Kumar, B.L., Choudhary, A.E., Kuznetsov, S.D., Kumar, S., et al.: Exploration of spectroscopic, surface morphological, structural, electrical, optical and mechanical properties of biocompatible PVA-GO PNCs. *Diam. Relat. Mater.* **127**, 109158 (2022)
- Devi, N., Ray, S.S.: Performance of bismuth-based materials for supercapacitor applications: a review. *Mater. Today Commun.* **25**, 101691 (2020)
- Devmande, B.H., Saurabh B. Somvanshi, Prashant B.K., and Madhukar B.S.: Rare earth ion (La³⁺) doped BaTiO₃ perovskite nanoceramics for spintronic applications. In: *Journal of Physics: Conference Series*, vol. 1644, no. 1, p. 012055. IOP Publishing (2020)

- Dhayal, V., Hashmi, S.Z., Kumar, U., Choudhary, B.L., Kuznetsov, A.E., Dalela, S., Kumar, S., Kaya, S., Dolia, S.N., Alvi, P.A.: Spectroscopic studies, molecular structure optimization and investigation of structural and electrical properties of novel and biodegradable Chitosan-GO polymer nanocomposites. *J. Mater. Sci.* **55**(30), 14829–14847 (2020)
- Ghosh, S., Dasgupta, S., Sen, A., Maiti, H.S.: Low temperature synthesis of bismuth ferrite nanoparticles by a ferrioxalate precursor method. *Mater. Res. Bull.* **40**(12), 2073–2079 (2005)
- Iqbal, M.F., Razaq, A., Ashiq, M.N., Kaneti, Y.V., Azhar, A.A., Yasmeen, F., Joya, K.S., Abbass, S.: Effect of graphene oxide thin film on growth and electrochemical performance of hierarchical zinc sulfide nanoweb for supercapacitor applications. *ChemElectroChem* **5**(18), 2636–2644 (2018)
- Iriani, Y., Sandi, D.K., Nurmawanti, R., Budiawanti, S., Agustina, E.B.: Microstructure and optical properties study of Nd-doped BiFeO₃ (Ba_{1-x}Nd_xFeO₃) films on quartz substrate. *Jurnal Penelitian Fisika dan Aplikasinya (JPFA)* **11**(2), 148–157 (2021)
- Jadhav, V.V., Zate, M.K., Liu, S., Naushad, M., Mane, R.S., Hui, K.N., Han, S.H.: Mixed-phase bismuth ferrite nanoflake electrodes for supercapacitor application. *Appl. Nanosci.* **6**(4), 511–519 (2016)
- Kalikeri, S., Shetty Kodialbail, V.: Auto-combustion synthesis of narrow band-gap bismuth ferrite nanoparticles for solar photocatalysis to remediate azo dye containing water. *Environ. Sci. Pollut. Res.* **28**(10), 12144–12152 (2021)
- Khajonrit, J., Wongprat, U., Kidkhunthod, P., Pinitsoontorn, S., Maensiri, S.: Effects of Co doping on magnetic and electrochemical properties of BiFeO₃ nanoparticles. *J. Magn. Magn. Mater.* **449**, 423–434 (2018)
- Khichar, K.K., Dangi, S.B., Dhayal, V., Kumar, U., Hashmi, S.Z., Sadhu, V., Choudhary, B.L., et al.: Structural, optical, and surface morphological studies of ethyl cellulose/graphene oxide nanocomposites. *Polym. Compos.* **41**(7), 2792–2802 (2020)
- Kibasomba, P.M., Dhlamini, S., Maaza, M., Liu, C.-P., Rashad, M.M., Rayan, D.A., Mwakikunga, B.W.: Strain and grain size of TiO₂ nanoparticles from TEM, Raman spectroscopy and XRD: the revisiting of the Williamson–Hall plot method. *Results Phys.* **9**, 628–635 (2018)
- Kock, I., Edler, T., Mayr, S.G.: Growth behavior and intrinsic properties of vapor-deposited iron palladium thin films. *J. Appl. Phys.* **103**(4), 046108 (2008)
- Kumar, V., Soam, A., Sahoo, P.K., Panda, H.S.: Enhancement of electrochemical properties of carbon solution doped bismuth ferrite for supercapacitor application. *Mater. Today: Proc.* **41**, 165–171 (2021a)
- Kumar, S., Srivastava, G., Almutairi, G., Ahmed, F., Shaalan, N.M., Dalela, S., Kumar, R., et al.: Electronic structure and electrochemical properties of La-doped BiFeO₃ nanoparticles. *J Electron Spectrosc. Relat. Phenom.* **253**, 147138 (2021)
- Kumar, S., Ahmed, F., Ahmad, N., Shaalan, N.M., Kumar, R., Alshoaibi, A., Arshi, N., et al.: Role of Cr doping on the structure, electronic structure, and electrochemical properties of BiFeO₃ nanoparticles. *Materials* **15**(12), 4118 (2022)
- Kumari, B., Mandal, P.R., Nath, T.K.: Magnetic, magnetocapacitance and dielectric properties of BiFeO₃ nanoceramics. *Adv. Mater. Lett.* **5**(2), 84–88 (2014)
- Kumari, A., Kumari, K., Aljawfi, R.N., Alvi, P.A., Dalela, S., Ahmad, M.M., Chawla, A.K., Kumar, R., Vij, A., Kumar, S.: Role of La substitution on structural, optical, and multiferroic properties of BiFeO₃ nanoparticles. *Appl. Nanosci.* **13**, 1–20 (2021)
- Kumari, A., Kumari, K., Ahmed, F., Ahmad, M.M., Sharma, J., Vij, A., Kumar, S.: Role of Bi-excess on structural, electrical, optical, and magnetic properties BiFeO₃ nanoparticles. *J. Mater. Sci.: Mater. Electron.* **32**(19), 23968–23982 (2021b)
- Kumari, A., Kavita, K., Ankush, V., Alvi, P.A., Shalendra, K.: Electrical and structural properties of La doped BiFeO₃. In: *AIP Conference Proceedings*, vol. 2220, no. 1, pp. 040032. AIP Publishing LLC (2020)
- Li, T., Hang, Yu., Zhi, L., Zhang, W., Dang, L., Liu, Z., Lei, Z.: Facile electrochemical fabrication of porous Fe₂O₃ nanosheets for flexible asymmetric supercapacitors. *J. Phys. Chem. C* **121**(35), 18982–18991 (2017)
- Liu, J., Chen, M., Zhang, L., Jiang, J., Yan, J., Huang, Y., Lin, Jianyi, Fan, H.J., Shen, Z.X.: A flexible alkaline rechargeable Ni/Fe battery based on graphene foam/carbon nanotubes hybrid film. *Nano letters* **14**(12), 7180–7187 (2014)
- Lokhande, C.D., Gujar, T.P., Shinde, V.R., Mane, Rajaram S., Han, Sung-Hwan.: Electrochemical supercapacitor application of pervoskite thin films. *Electrochem. Commun.* **9**(7), 1805–1809 (2007)
- Manzoor, A., Afzal, A.M., Umair, M., Ali, A., Rizwan, M., Yaqoob, M.Z.: Synthesis and characterization of Bismuth ferrite (BiFeO₃) nanoparticles by solution evaporation method. *J. Magn. Magn. Mater.* **393**, 269–272 (2015)

- Matinise, N., Botha, N., Madiba, I.G., Maaza, M.: Mixed-phase bismuth ferrite oxide (BiFeO_3) nanocomposites by green approach as an efficient electrode material for supercapacitor application. *MRS Adv.* **8**, 1–5 (2023)
- Mauger, A., Julien, C., Paoletta, A., Armand, M., Zaghbi, K.: Recent progress on organic electrodes materials for rechargeable batteries and supercapacitors. *Materials* **12**(11), 1770 (2019)
- Miriyala, N., Prashanthi, K., Thundat, T.: Oxygen vacancy dominant strong visible photoluminescence from BiFeO_3 nanotubes. *Phys. Status Solidi* **7**, 668–671 (2013)
- Moharana, S., Yadav, T., Alvi, P.A., Pathak, A., Mahaling, R.N.: Enhanced dielectric and electrical properties of tri-phase percolative PVDF– BiFeO_3 –carbon black (CB) composite film. *J. Mater. Sci.: Mater. Electron.* **32**, 6038–6046 (2021)
- Mote, V.D., Purushotham, Y., Dole, B.N.: Williamson–Hall analysis in estimation of lattice strain in nanometer-sized ZnO particles. *J. Theor. Appl. Phys.* **6**, 11–8 (2012)
- Nayak, A.K., Gopalakrishnan, T.: Phase-and crystal structure-controlled synthesis of Bi_2O_3 , Fe_2O_3 , and BiFeO_3 nanomaterials for energy storage devices. *ACS Appl. Nano Mater* **5**(10), 14663–14676 (2022)
- Rajae, A., Wensheng, X., Zhao, L., Wang, S., Liu, Y., Wu, Z., Si-Shen, F.: Multifunctional bismuth ferrite nanoparticles as magnetic localized dose enhancement in radiotherapy and imaging. *J. Biomed. Nanotechnol.* **14**(6), 1159–1168 (2021)
- Sarma, B., Jurovitzki, A.L., Smith, Y.R., Mohanty, S.K., Misra, M.: Redox-induced enhancement in interfacial capacitance of the titania nanotube/bismuth oxide composite electrode. *ACS Appl. Mater. Interfaces.* **5**(5), 1688–1697 (2013)
- Scherrer, P.J.G.W.G.: Bestimmung der Grösse und der inneren von Kolloidteilchen mittels Röntgenstrahlen. *Struktur Nachr. Ges Wiss Göttingen* **26**, 98–100 (1918)
- Sharma, P., Kumar, V.: Current technology of supercapacitors: a review. *J. Electron. Mater.* **49**(6), 3520–3532 (2020)
- Sharma, M., Aljawfi, R.N., Kavita Kumari, K.H., Chae, S., Dalela, S., Gautam, P.A., Alvi, P.A., Kumar, S.: Investigation of local geometrical structure, electronic state and magnetic properties of PLD grown Ni doped SnO_2 thin films. *J. Electron Spectrosc. Relat. Phenom.* **232**, 21–28 (2019)
- Sheng, H., Zhang, X., Liang, J., Shao, M., Xie, E., Cunjiang, Yu., Lan, W.: Recent advances of energy solutions for implantable bioelectronics. *Adv. Healthcare Mater.* **10**(17), 2100199 (2021)
- Somwanshi, S.B., Somvanshi, S.B., Kharat, P.B., Thorat, N.D.: Magnetically retrievable Fe-doped TiO_2 nanoparticles for photo-induced toxic dye removal applications. In *Macromol Symp* **400**(1), 2100112 (2021)
- Somwanshi, S.B., Somvanshi, S.B., Kharat, P.B.: Visible light driven photocatalytic activity of TiO_2 nanoparticles prepared via gel-combustion process. In: *Journal of Physics: Conference Series*, vol. 1644, no. 1, pp. 012042. IOP Publishing (2020)
- Vivier, V., Régis, A., Sagon, G., Nedelec, J.-Y., Yu, L.T., Cachet-Vivier, C.: Cyclic voltammetry study of bismuth oxide Bi_2O_3 powder by means of a cavity microelectrode coupled with Raman microspectrometry. *Electrochim. Acta* **46**(6), 907–914 (2001)
- Vyas, A., Hajibagher, S.Z., Romero, U.M., Azega, R.K., Wang, E., Lundgren, P., Enoksson, P., Smith, A.D.: Alkyl-amino functionalized reduced-graphene-oxide–heptadecan-9-amine-based spin-coated microsupercapacitors for on-chip low power electronics. *Phys. Status Solidi* **259**(2), 2100304 (2022)
- Wang, Y., Gang, Xu., Ren, Z., Wei, X., Weng, W., Piyi, Du., Shen, Ge., Han, G.: Mineralizer-assisted hydrothermal synthesis and characterization of BiFeO_3 nanoparticles. *J. Am. Ceram. Soc.* **90**(8), 2615–2617 (2007)
- Wang, Y., Gang, Xu., Ren, Z., Wei, X., Weng, W., Piyi, Du., Shen, Ge., Han, G.: Low temperature polymer assisted hydrothermal synthesis of bismuth ferrite nanoparticles. *Ceram. Int.* **34**(6), 1569–1571 (2008)
- Wang, Y., Gang, Xu., Yang, L., Ren, Z., Wei, X., Weng, W., Piyi, Du., Shen, Ge., Han, G.: Low-temperature synthesis of $\text{Bi}_2\text{Fe}_4\text{O}_9$ nanoparticles via a hydrothermal method. *Ceram. Int.* **35**(1), 51–53 (2009)
- Wang, D., Wang, M., Liu, F., Cui, Y., Zhao, Q., Sun, H., Jin, H., Cao, M.: Sol–gel synthesis of Nd-doped BiFeO_3 multiferroic and its characterization. *Ceram. Int.* **41**(7), 8768–8772 (2015)
- Wang, F.L., Li, Y., Wang, N., Zhu, L., Jain, A., Wang, Y.G., Chen, F.G.: Enhanced magnetic, ferroelectric and optical properties of Sr and Co co-doped BiFeO_3 powders. *J. Alloy. Compd.* **810**, 151941 (2019)
- Wu, J., Fan, Z., Xiao, D., Zhu, J., Wang, J.: Multiferroic bismuth ferrite-based materials for multifunctional applications: ceramic bulks, thin films and nanostructures. *Prog. Mater. Sci.* **84**, 335–402 (2016)
- Wu, H., Xue, P., Yao, Lu., Zhu, X.: Microstructural, optical and magnetic characterizations of BiFeO_3 multiferroic nanoparticles synthesized via a sol-gel process. *J. Alloy. Compd.* **731**, 471–477 (2018)
- Yan, F., Zhu, T.J., Lai, M.O., Lu, L.: Enhanced multiferroic properties and domain structure of La-doped BiFeO_3 thin films. *Scripta Mater.* **63**(7), 780–783 (2010)

Zhang, F., Zeng, X., Bi, D., Guo, K., Yao, Y., Shengguo, Lu.: Dielectric, ferroelectric, and magnetic properties of Sm-doped BiFeO₃ ceramics prepared by a modified solid-state-reaction method. *Materials* **11**(11), 2208 (2018)

Publisher's Note Springer Nature remains neutral with regard to jurisdictional claims in published maps and institutional affiliations.

Springer Nature or its licensor (e.g. a society or other partner) holds exclusive rights to this article under a publishing agreement with the author(s) or other rightsholder(s); author self-archiving of the accepted manuscript version of this article is solely governed by the terms of such publishing agreement and applicable law.

Authors and Affiliations

Garima Srivastava¹ · Shalendra Kumar² · S. Z. Hashmi³ · Ravina¹ · A. M. Quraishi⁴ · Saurabh Dalela⁵ · Faheem Ahmed⁶ · Kavita Kumari⁷ · B. H. Koo⁷ · P. A. Alvi¹

✉ Shalendra Kumar
shiluphy@gmail.com

✉ P. A. Alvi
drpaalvi@gmail.com

¹ Department of Physical Science, Banasthali Vidyapith, Banasthali, Rajasthan 304022, India

² Department of Physics, University of Petroleum and Energy Studies, Dehradun, Uttarakhand 248007, India

³ Department of Chemistry, Banasthali Vidyapith, Banasthali 304022, Rajasthan, India

⁴ Department of Electrical Engineering, College of Engineering, Qassim University, Unaizah, Saudi Arabia

⁵ Department of Pure and Applied Physics, University of Kota, Kota, Rajasthan 324005, India

⁶ Department of Physics, College of Science, King Faisal University, P.O. Box 400, 31982 Hofuf, Al-Ahsa, Saudi Arabia

⁷ School of Materials Science and Engineering, Changwon National University, Changwon 51140, Gyeongnam, Korea